

# Study of low-frequency quasi-periodic oscillations in GRS 1739–278 during 2014 outburst

Ilya A. Mereminskiy<sup>1\*</sup>, Andrey N. Semena<sup>1</sup>, Alexander A. Lutovinov<sup>1</sup>,  
Sergey D. Bykov<sup>1,2</sup>, Ekaterina V. Filippova<sup>1</sup>

<sup>1</sup>*Space Research Institute, Russian Academy of Sciences, Moscow, Russia*

<sup>2</sup>*Bauman Moscow State Technical University, Moscow, Russia*

Accepted XXX. Received YYY; in original form ZZZ

## ABSTRACT

We detected a type-C LF QPO at 0.3–0.7 Hz in *NuSTAR* and *Swift-XRT* observations of the black hole candidate GRS 1739–278 during the hard-intermediate state of its 2014 outburst. We traced the evolution of spectro-timing properties of the source during *NuSTAR* observation. As QPO frequency increases, the source spectrum becomes softer, with increasing power-law index and decreasing cut-off energy.

We performed an extended analysis of rapid X-ray variability in terms of power spectrum, cospectrum, coherence and phase-lags. In the power spectrum a prominent QPO and its second harmonic are clearly seen. The fluxes in soft and hard X-ray bands are coherent, however coherence drops the separation of the energy bands. Phase-lags are generally positive (hard) in the 0.1–3 Hz frequency range, and negative below 0.1 Hz. Measurements of the inner disk radius obtained with the spectral models accounting for the metric around black hole and QPO frequency together with the relativistic precession model points towards very massive black hole.

**Key words:** X-rays: individual (GRS 1739–278) – X-rays: binaries – accretion, accretion disks – stars: black holes

## 1 INTRODUCTION

A study of X-ray variability in accreting astrophysical sources provides a broad view on processes that take a place in such systems. This works both on a long timescales - i.e. days and weeks - when one speaks about state changes through outbursts of transients sources (see e.g. [Homan and Belloni 2005](#); [Heil et al. 2015](#)), and on short - all the way down to milliseconds - when the subject under consideration are a quasi-periodic oscillations (QPOs) and broad band stochastic noise. By simultaneous usage of spectral and timing data one can better constrain geometry of accretion flow around compact objects and infer on which processes are responsible for generation of observed spectro-timing features in a self-consistent way.

Some aspects of the spectro-timing evolution of X-ray transients (usually black-hole candidates, BHC) during outbursts can be explained in the frame of the two-temperature accretion flow model ([Eardley et al. 1975](#); [Shapiro et al. 1976](#); [Narayan and Yi 1995](#)), in which it is proposed that the accretion flow in a system consists of the geometrically thin cold disk and geometrically thick hot flow (corona). It is

strongly suggested from the observations that this geometrically thick hot flow is responsible for production of strong variability. As an example, using frequency-resolved spectroscopy [Churazov et al. \(2001\)](#) shown that variable part of the emission from the BHC system Cyg X-1 has a hard power-law shaped spectrum, which is thought to be produced by Comptonization of soft photons onto hot electrons in the corona, while stable part of the emission has a spectrum which is consistent with the cold classical  $\alpha$ -disc spectrum ([Shakura and Sunyaev 1973](#)). It is also well known that total variability power of BHC and neutron star binaries is greater in the hard state (when the spectrum is dominated by the emission produced in the hot flow) than in the soft state (when the spectrum can be described with optically thick  $\alpha$ -disc model) ([Miyamoto et al. 1992](#); [Revnivtsev et al. 2000](#); [Homan et al. 2001](#); [Churazov et al. 2001](#), e.t.c.). [Lyubarskii \(1997\)](#) proposed that observed strong variability (seen as a broad band noise in power spectra) is produced due to the stochastic variations of the angular momentum transport efficiency. In this propagating fluctuation model broad band noise of the luminosity is a product of noise signals from different radii of the accretion flow, each with its own characteristic time-scale (see, e.g. [Arévalo and Uttley 2006](#); [Ingram and van der Klis 2013](#)). Therefore, the spectral

\* E-mail: i.a.mereminskiy@gmail.com

shape of the broad band noise is determined by the physical and geometrical properties of the accretion flow, e.g. in particular in these works it was suggested that the broad noise dumping frequency is connected to the inner edge of the accretion flow.

Another feature, frequently observed in the X-ray binaries power spectra is different types of low and high frequency QPOs, manifesting itself as a narrow Lorentzian components (see Casella et al. 2005; Belloni and Motta 2016, for LFQPO classification) at frequencies of few mHz – 30 Hz. This QPOs are ubiquitous - they found in systems with neutron stars and black holes (Wijnands and van der Klis 1999), in cataclysmic variables (Mauche 2002) and even in active galactic nuclei (Gierliński et al. 2008). Their origin still remains unclear, although it is possible that different mechanisms are responsible for different types of QPO.

Type-C LF QPOs typically found in X-ray black hole transients during initial rise and transition to disk dominated state - i.e. in low-hard state (LHS) and in hard intermediate state (HIMS), according to standard scheme (Grebenev et al. 1997; Tanaka and Shibazaki 1996; Remillard and McClintock 2006; Belloni 2010), although it is sometimes seen at higher frequencies ( $\approx 30$  Hz) after transition to high soft state (HSS). These QPOs are easy to detect and study, since they occur at moderate frequencies of 0.1–10 Hz and prominent, having  $rms \approx 10\%$ . Different authors prescribe generation of these QPOs to various processes: Lense-Thirring precession of inner parts of the accretion disk (Stella and Vietri 1998; Ingram et al. 2009), oscillations of a standing shock (Molteni et al. 1996) and accretion rate modulation caused by different phenomena (Tagger and Pellat 1999; Cabanac et al. 2010) e.t.c. In some models, particularly in relativistic precession models (RPM), observed frequency is strongly dependent on the inner radius of the accretion disk, at which it transforms into geometrically thick optically thin hot flow.

Recent advances in simulations of the reflected emission (Ross and Fabian 2005; García et al. 2014), arising due to the scattering and absorption of the hard photons in the cold accretion disk, led to the possibility to study geometry of the disk. For such a study to be made it is essential to obtain broadband X-ray spectrum with high energy resolution - reflected emission manifest itself by a presence of prominent, wide and asymmetric iron  $K_\alpha$  fluorescent emission line at 6.4 keV and Compton-hump at 20–30 keV. Now, adding information from X-ray timing one can, in principle, constrain the location of a component, responsible for the variability - which is though to be a corona or a jet base. This task presents a challenge, that can be solved only by a telescope that posses both possibility to measure a broadband spectrum with good resolution and have a corresponding timing capabilities. *NuSTAR* (Harrison et al. 2013), launched in 2013, is the best available instrument for such studies. *XMM-Newton* and *NICER* can be used too, yet they energy range reaching only up to  $\sim 12$  keV limits their capability to measure hard tails and Compton-hump contribution. Nevertheless there are some great results obtained with these instruments, e.g. measurement of the Fe  $K_\alpha$  line profile variation with QPO phase by Ingram et al. (2016).

In this article we report on first detection of type-C QPOs in HIMS of Galactic black-hole candidate GRS 1739–

278 and present a detailed study of properties of the X-ray variability, along with spectral evolution.

## 2 GRS 1739-278

GRS 1739–278 is a typical X-ray nova, discovered during outburst in 1996 (Paul et al. 1996) by *SIGMA* (Paul et al. 1991) telescope onboard *GRANAT* space observatory. Using *ROSAT* observation from the estimated absorption Greiner et al. (1996) inferred distance of 6–8.5 kpc, indicating that the source may belong to Galactic bulge. It should be noted that Greiner et al. (1996) used X-ray halo size to assess obscuration column density, and mean extinction per parsec value from (Allen 1973) to estimate distance to the source. While his  $N_H$  estimation appears to be quite precise, new measurements of the obscuration in the Galaxy (Dickey and Lockman 1990; Kalberla et al. 2005; Marshall et al. 2006; Schultheis et al. 2014) shows that the source either has intrinsic obscuration or additional line of sight obscuration, but the distance can not be constrained, since the line of sight obscuration in Galaxy towards the source is smaller than its estimated  $N_H$ . Nevertheless in this work we will assume that the distance to GRS 1739–278 is 8 kpc, given that the source is projected on to the Galactic Bulge.

Optical and radio emission were detected during the course of outburst (Hjellming et al. 1996; Marti et al. 1997). Borozdin et al. (1998) found spectral evolution throughout the outburst to be consistent with canonical model - outburst starts from LHS, then soft emission, associated with the optically thick disk starts to dominate, heralding transition to high soft state. Eventually, they observed very high state and detected a QPO at 5 Hz using *RXTE* data (Borozdin and Trudolyubov 2000; Wijnands et al. 2001).

After some 18 year slumber GRS 1739–278 demonstrated another big outburst, rise of which was detected by *Swift-BAT* (Krimm et al. 2014) along with *INTEGRAL* (Filippova et al. 2014). During this outburst extensive observing campaign by *Swift-XRT* were carried out, along with single long *NuSTAR* exposure. After this outburst the source remain active with repetitive mini-outbursts (Mereminskiy et al. 2017; Yan and Yu 2017).

## 3 OBSERVATIONS AND DATA REDUCTION

In order to characterize the overall outburst profile we used data of *Swift-BAT transient monitor* (Krimm et al. 2013) in hard X-rays (15–50 keV) as well as data from *MAXI* (Matsuoka et al. 2009) (2–4 keV).

We used *NuSTAR* observation (ObsID: 80002018002) performed at March 26, 2014 (MJD 56742). *nuproducts* pipeline were utilized to extract photons from two-arcminute circular region, centered on the source and to produce lightcurves and spectra.

We also used public observations of *Swift-XRT* (target ID: 33203) performed regularly over the peak and decline of the outburst. Since the source was bright, all *Swift-XRT* observations were performed in windowed mode, allowing study of timing properties of the source. We performed standard analysis with *xrtpipeline* and barycentered data prior

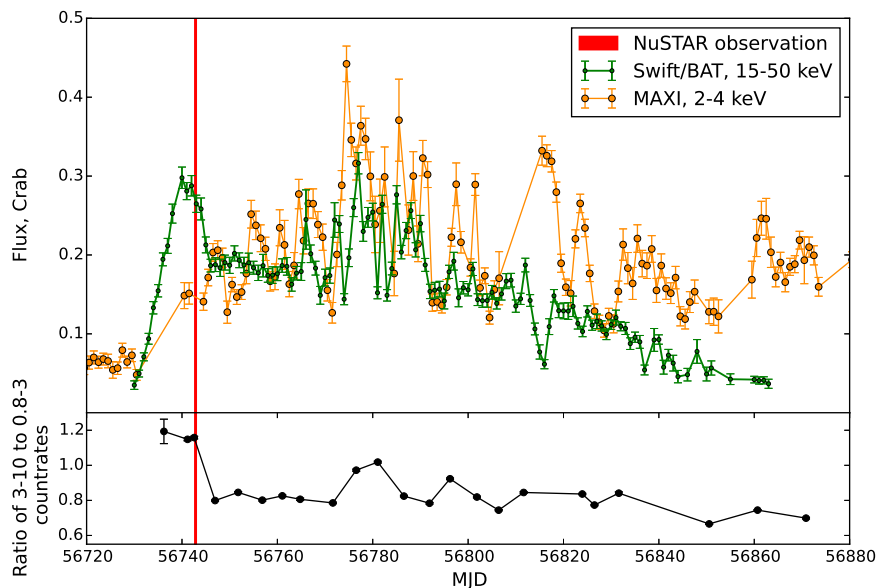


**Figure 1.** *Upper:* green points denote *Swift-BAT* lightcurve of 2014 outburst in 15–50 keV range, orange circles correspond to *MAXI* fluxes in 2–4 keV. Red line show the time interval of *NuSTAR* observation. *Lower:* evolution of *Swift-XRT* spectral hardness during the outburst.

to lightcurve extraction. During several observations count-rate was as high as  $280 \text{ cts s}^{-1}$ , therefore we excluded one or few brightest columns depending on count-rate, in order to suppress effects caused by photon pile-up. Photons with energies below 0.8 keV and above 10 keV were also filtered out. Long-term lightcurves and spectra were obtained from UK Swift Science Data Centre at the University of Leicester (Evans et al. 2009).

## 4 ANALYSIS

### 4.1 Outburst

First detection of the source by *Swift-BAT* (Krimm et al. 2014) occurred at March 9, 2014 (MJD 56725, we will refer to this date as  $\tau_0$ ). Outburst profile in hard X-rays (15–50 keV) featured fast rise with tenfold intensity increasing over ten days, nearly flat-top peak ( $\tau_0+10..+15$  days) followed by abrupt flux decrease by 30% over two days. After this, the source demonstrated gradual decline interrupted by flaring activity at  $\tau_0+30..+65$  days. Another interesting feature is a dip, observed in *Swift-BAT* lightcurve at  $\tau_0 \approx +86$  days. After the cease of the outburst source remained active with flux about 5–15 mCrab.

Adding data from *MAXI* to the *Swift-BAT* hard X-ray lightcurve gives us another insight on the outburst evolution as shown in Fig. 1 – comparing fluxes in soft and hard bands (for 2–4 keV band we took a  $1.67 \text{ counts s}^{-1}$  as a reference value for Crab, corresponding value for 15–50 keV band is  $0.22 \text{ cts cm}^{-2} \text{ s}^{-1}$ ) one can see that the soft component obviously lags hard emission in the beginning of the outburst but then starts to grow and ends up dominating during the flaring period as well as during hard dip. Lower subplot of Fig. 1 shows evolution of hardness ratio (3–10 keV/0.8–3 keV) measured by *Swift-XRT*. Right after the peak of hard

emission one can see the decline of hardness, also indicating appearance of the thermal component. For a detailed analysis of the spectral evolution during the outburst see citep[[in preparation]bykov18.

Fortunately, *NuSTAR* observation triggered by Miller et al. (2015) were carried right at the transition between hard and soft states, thus giving us unique possibility to study processes that happens during HIMs.

### 4.2 NuSTAR observation

*NuSTAR* observed GRS 1739–278 for nearly 30 ks of net exposure right after the hard X-ray peak (see Fig. 1). Earlier, Miller et al. (2015) shown that the average spectrum of this observation is well described by reflection models such as *relxill* (García et al. 2014; Dauser et al. 2014, 2016) with accretion disk that reaches remarkably close to the black hole innermost stable circular orbit (ISCO), with disk inner edge radius upper estimate being  $R_{\text{in}} = 5^{+3}_{-4} GM/c^2$  (Miller et al. 2015). They also noted, that no additional thermal component was needed in order to describe *NuSTAR* energy spectrum probably due to the low disk temperature and high absorption.

Given the 96.9 minute orbital period of *NuSTAR*, observation is divided in 13 intervals separated by Earth occultations, as shown in Fig. 2. We denoted these intervals with roman numerals, from **I** to **XIII**. From the lightcurve of observation it is clear, that the source flux is increasing throughout observation from  $\approx 145$  up to  $\approx 170$  counts per second. The spectrum also alter, with hardness (defined as ratio of count rates  $R_{3-10 \text{ keV}}/R_{10-78 \text{ keV}}$ ) monotonically growing from 2.7 to 3.1.

#### 4.2.1 Continuum evolution

To get better view on the evolution of continuum emission we fitted all individual interval spectra using XSPEC package (Arnaud 1996) with absorbed `xillver` (García et al. 2013) model (`const*phabs*xillver`). This model describes reflection of incident radiation from ionized slab of matter. The spectrum of incident radiation are assumed to be power-law with exponential cutoff. We peaked `xillver` model over the `relxill` for separate intervals analysis because we wanted to describe the changes in the continuum emission making no assumptions on the system geometry.

Spectra from two *NuSTAR* modules of each interval were fitted simultaneously with free cross-calibration constant between modules. We choose to fix interstellar absorption at  $N_H = 2.15 \times 10^{22} \text{ cm}^{-2}$  as was found by joint *XMM-Newton*/*NuSTAR* observation during low luminosity state (Fuerst et al. 2016). Element abundances were taken from Wilms et al. (2000) and cross-sections from Verner et al. (1996). Relative iron abundance were fixed at  $A_{Fe} = 1$ , ionization parameter at  $\xi = 3.2$  and inclination at 35 degrees, in consistency with Miller et al. (2015) results obtained with different spectral models. Although in `xillver` there is no relativistic broadening of Fe  $K\alpha$  emission line no significant residuals in 5–8 keV region are seen, mainly because of limited statistics in per interval spectra. Before fitting, spectra were grouped in order to have at least 100 counts per bin, channels above 60 keV were ignored. Resulting fits are of satisfactory quality with  $\chi^2_{red} \approx 1.05$ .

Examination of the best-fit parameters (see Table 2 and Fig. 4) confirms that the spectrum softens during the observation and the cut-off energy decreases.

#### 4.2.2 Constrains on movement of the inner parts of accretion disk

Spectra of single intervals have not enough statistics to constrain change of Fe-line profile and, hence, to determine whether the disk inner boundary is moving during observation. To increase statistics, we split whole observation into three major pieces, with first made by intervals **I–IV**, second by **V–IX** and third by **X–XIII** and extracted 4–78 keV spectra. We chose to group them in order to have at least 100 counts per bin and then we fitted them (excluding data between 5–10 keV) with simple `phabs*cutoffpl` model, using, once again,  $N_H = 2.15 \times 10^{22} \text{ cm}^{-2}$ .

Now, plotting the ratio of this fit to initial spectra (see Fig. 3) one can see that both strong features - i.e. Fe-line complex at 5–9 keV and Compton hump around 30 keV are seemingly stable. Therefore we can conclude, that there is no drastic change in position of inner disk boundary between parts of observation. Additionally, we estimated the equivalent width of Fe  $K\alpha$  emission line in this three parts - we approximated 4–78 keV spectra with 10–30 keV range being ignored (to neglect the Compton-hump contribution) with model consisting of absorbed cut-off powerlaw and gaussian. Equivalent width of the gaussian component is around 0.175 keV and remains constant along the observation within error margins, although it is possible that the quality of data is not enough to trace the real change.

#### 4.2.3 Average spectrum analysis

There is a 1.3 ks part of *Swift-XRT* snapshot (ObsId: 00033203003) that coincides with *NuSTAR* observation. Extension of an energy range to 0.8–78 keV allows one to search for thermal emission associated with the cold inner disk with  $kT \sim 0.1\text{--}0.4$  keV (such as were found in other BHCs, see (Miller et al. 2006a,b; Parker et al. 2015, et.c)).

We extracted *Swift-XRT* spectrum using only zero-grade events, grouped it to has at least 30 counts per bin and added 3% systematic error. Similar grouping were applied to *NuSTAR* data.

Since the average spectrum has much better statistics we will apply more sophisticated `relxillp` spectral model that describes reflection of emission produced by point source located on the rotation axis above the Kerr black hole from the relativistic accretion disk. We used latest available version of `relxillp` package (v1.0.2). Jet foundation are often thought to be responsible for this type of “lamp-post” geometry. Among the parameters of a model several are of a particular interest, namely  $h$  - height of a point source above the black hole illumination the accretion disk and  $R_{in}$  - its inner radius. We selected this model for several reasons - first, Miller et al. (2015) found that it matches *NuSTAR* data well. Also, during the 1996 outburst source was detected at radiowaves, possibly indicating jet activity. For spectral fitting we used `migrad` minimizer from *MINUIT* package (James and Roos 1975), and in order to estimate errors we employed a large MCMC chain.

Interestingly, instead of surplus thermal component we found a lack of the soft emission - usage of  $N_H = 2.15 \times 10^{22} \text{ cm}^{-2}$ , measured in the low state (Füerst et al. 2016) led to worse fits with systematic negative residuals below few keV. Therefore, we left  $N_H$  free during the fit. Obtained value of  $2.64 \times 10^{22} \text{ cm}^{-2}$  is higher than one measured by Füerst et al. (2016). This can be possibly accounted to a presence of disk outflow, caused by severe X-ray irradiation.

Obtained upper limit on truncation radius of accretion disk -  $r_{in} < 9GM/c^2$  (90% confidence limit) is similar to the value from Miller et al. (2015), height of the source above the accretion disk is in agreement too (see Tab. 1 for obtained parameters). Some discrepancy seen in the parameters of accretion disk - e.g. inclination, ionization parameter and Fe-abundance, it can be caused by broader energy range. As it can be seen from Fig. 5 there is no significant residuals in lower-energy part of the spectrum, therefore thermal emission from accretion disk is too weak or too cold to detect.

Total unabsorbed flux in 0.1–100 keV band is about  $1.4 \times 10^{-8} \text{ erg s}^{-1} \text{ cm}^{-2}$  which translates to a luminosity of  $1.1 \times 10^{38} \text{ erg s}^{-1}$  for the 8 kpc distance. Typical luminosity at which BHCs change from LHS to HIMS is about  $0.1L_{Edd} = 1.2 \times 10^{37} (M/M_\odot) \text{ erg s}^{-1}$ , although we should note that there is significant scatter in this value. Therefore one can put a rough lower estimate on the black-hole mass as  $9 M_\odot$ , which is reasonable.

## 5 TIMING ANALYSIS

Variability properties of different types of X-ray binary systems are usually described in terms of the power spectrum. Power spectrum of the BHC systems in LHS typically can

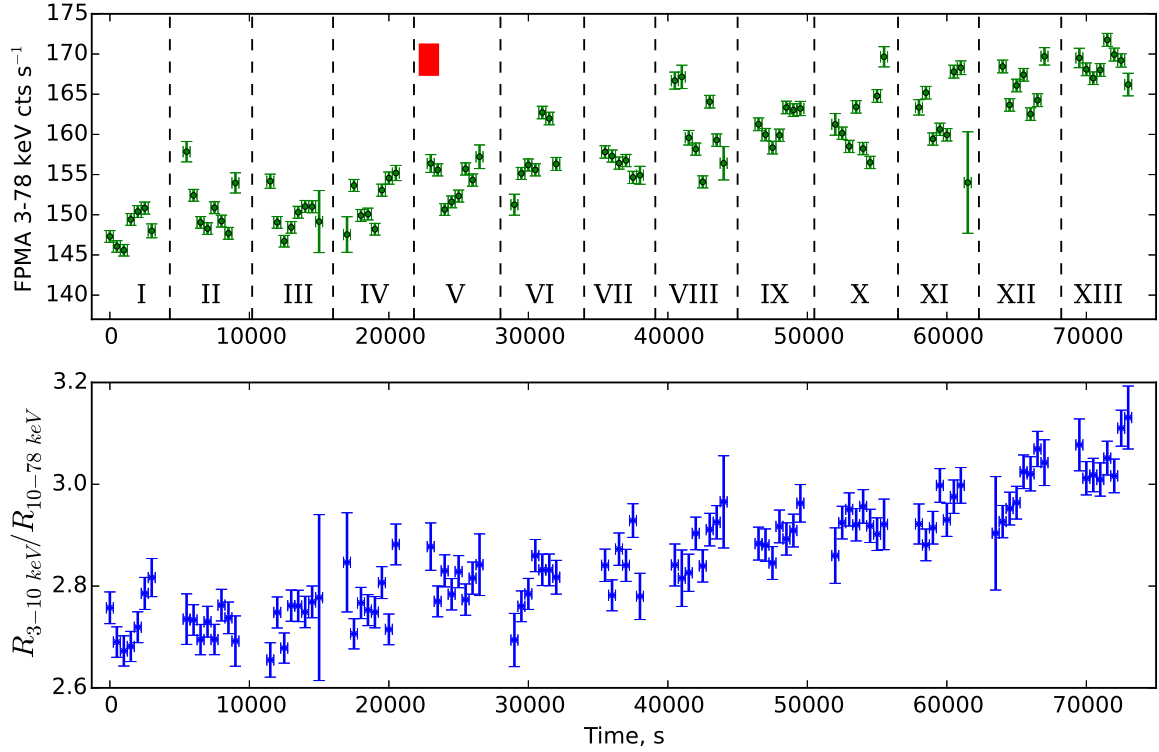


**Figure 2.** Upper panel: countrate of *NuSTAR* FPMA in 3–78 keV band. We enumerated intervals of uninterrupted observations with roman numerals. Red square shows time of simultaneous *Swift-XRT* observation (ObsId: 00033203003, second part). Bottom panel: evolution of hardness during observation

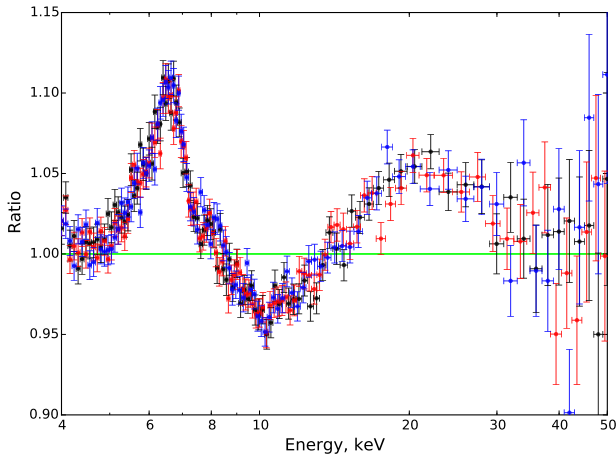


**Figure 3.** Ratio of *NuSTAR* FPMA spectra to *phabs\*cutoffpl* model. In black - data from intervals I–IV, in red from V–IX and in blue from X–XIII.

be described as a combination of a band-limited noise and one or few narrow Lorentzian functions, representing QPOs (see, e.g. Terrell 1972; Belloni and Hasinger 1990; Homan and Belloni 2005, e.t.c). Properties of this components and correlations between them, in principle, may be used to discriminate between different models, proposed for generation of X-ray emission in BHC.

Although power spectra analysis is by far the most pop-

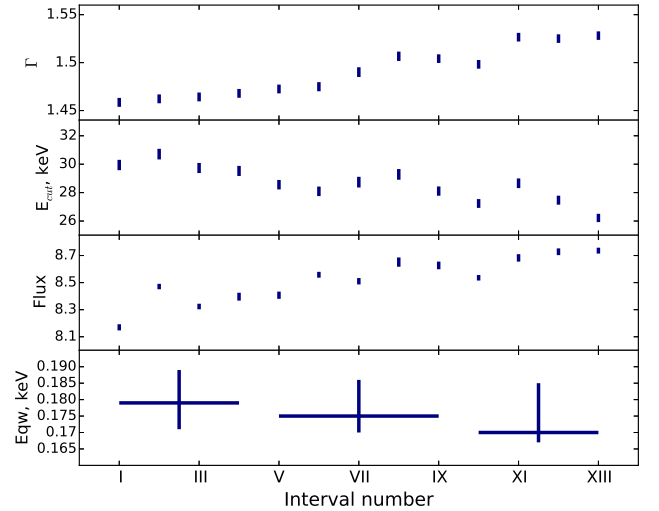


**Figure 4.** Parameters of continuum emission in intervals. From upper to lower: *xillver* powerlaw slope, cutoff energy, flux in 3–60 keV band  $\times$   $\text{erg s}^{-1} \text{cm}^{-2}$  and Fe-line equivalent width.

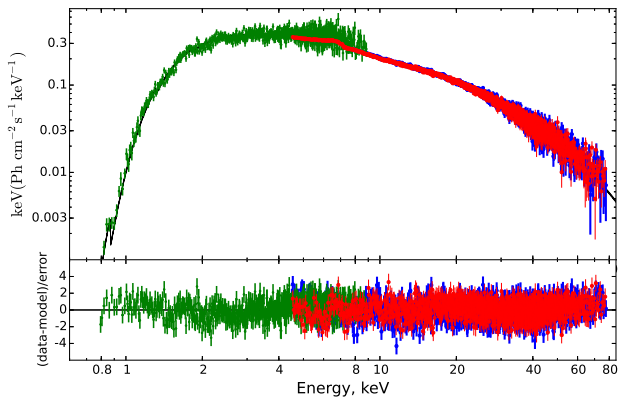
ular, more sophisticated methods, such as coherence function or phase-lag were successfully used to infer physical properties of accretion flows. Using a measured time-lag between the soft and hard emission, which has a complex behavior with the frequency Nowak et al. (1999) constrained geometrical size of the accretion flow.

In the following section we present analysis of the



**Table 1.** Best-fit parameters of `phabs*relxilllp` model

Parameter	Value
$N_H, 10^{22} \text{ cm}^{-2}$	$2.64^{+0.05}_{-0.03}$
$h, GM/c^2$	$22.3^{+0.6}_{-4.3}$
$a, cJ/GM^2$	$0.73^{+0.26}_{-0.23}$
$incl, \text{deg}$	$22.1^{+2.9}_{-2.0}$
$R_{in}, ISCO$	$1.05^{+1.73}_{-0.02}$
$\Gamma$	$1.40^{+0.01}_{-0.01}$
$\log \xi$	$3.52^{+0.05}_{-0.07}$
$A_{Fe}$	$3.0^{+0.6}_{-0.3}$
$E_{cut}, \text{keV}$	$26.3^{+0.3}_{-0.5}$
$R_{refl}$	$0.42^{+0.03}_{-0.03}$
$N_{FMPA}, \times 10^{-2}$	$1.49^{+0.09}_{-0.03}$
$C_{FMPB}$	$1.017^{+0.002}_{-0.001}$
$C_{Swift-XRT}$	$1.04^{+0.01}_{-0.01}$
$\chi^2_{red.}$	1.1 =
	= 3366.21/3062 d.o.f

**Figure 5.** Fit of composite *Swift-XRT*/*NuSTAR* spectrum by `phabs*relxilllp` model. Green, red and blue points correspond to *Swift-XRT*, *NuSTAR* FPMA and FPMB, correspondingly.

GRS 1739–278 timing properties and their evolution during the 2014 outburst.

### 5.1 Power spectrum

We split *NuSTAR* observation of the GRS 1739–278 2014 outburst on 13 continuous intervals separated with  $\sim 0.7$  hr intervals when the source was occulted by Earth. The continuous intervals have duration from  $\sim 2440$  to  $\sim 3390$  sec see Table 2. Since *NuSTAR* detectors operate in the photons counting mode, data can be reduced to the light-curve with time resolution up to  $2\mu\text{s}$ . For our analysis we extracted light-curves with 0.01 s temporal resolution in a few energy bands (3–78, 3–10, 3–5, 5–8, 8–15, 15–78, 10–78 keV), which allows us to examine  $\sim 3 \times 10^{-3}$ –50 Hz frequency range. As it was mentioned above, this is a frequency band which usually contains low frequency QPOs and broad band noise (Wijnands and van der Klis 1999).

*NuSTAR* detectors are subject to non-paralyzing dead time with characteristic timescale  $\tau \approx 2.5 \mu\text{s}$  (Bachetti et al. 2015), in our case the effects from dead-time are already

present at frequencies above 20 Hz. Bachetti et al. (2015) noted that *NuSTAR* dead-time has a complex dependence on the energy of registered photons, and therefore it is hard to create analytical model for resulting power spectra. They proposed to use the real part of the cross spectrum of light-curves obtained from two *NuSTAR* detectors for the estimation of the power spectrum

$$re(F_{\text{FPMA}}^* F_{\text{FPMA}}) \quad (1)$$

where  $F_{\text{FPMA[B]}}$  - Fourier function of a light curve from FPMA[B] module, \* - stands for complex conjugation.

This method is based on the following assumption: signals produced by an observed source on two detectors are identical and have no time lag and therefore their Fourier functions are also identical and have zero phase shift, in contrast, signals independent for two detectors (like counting statistics) have random phase shifts. It follows that for independent signals the average real part of the cross spectrum tends to zero due to the random phase shift.

Huppenkothen and Bachetti (2017) shown that the cross-spectrum (or shortly cospectrum) in each frequency bin is distributed with Laplace probability density function (PDF) if it is derived from two normally distributed random independent series (see, e.g. 14 in Huppenkothen and Bachetti 2017):

$$p(C_j|0, \sigma_x \sigma_y) = \frac{1}{\sigma_x \sigma_y} \exp\left(\frac{-|C_j|}{\sigma_x \sigma_y}\right) \quad (2)$$

Where  $C_j$  - cospectrum of two *uncoherent* series measured in the  $j$ -th frequency channel and  $\sigma_x, \sigma_y$  - are second momenta of the initial normal distributions (therefore they are equal to the square of the power spectra in corresponding frequency channel for each time series). If signals used for the cospectrum estimation have identical power spectra then  $\sigma_x = \sigma_y \approx |F_{\text{FPMA}}|$ . We, therefore, see that to determine proper likelihood function which can be used to approximate cospectra with analytical functions, one still has to know Poisson noise level. It is also worth noting, that source count-rate and total count-rate are usually slightly differs for two *NuSTAR* modules making amplitudes of counting-statistic and dead-time not equal. Taking all this arguments into consideration we decided to use standard power spectrum for our analysis.

Since we used relatively large time binning (10 ms) to extract lightcurves from *NuSTAR* data and also usually considered variability at frequencies below 10 Hz, we assumed that the only effect from the dead-time is lowering of the constant Poisson noise level on the  $(1 - 2\nu\tau_d)$  factor, where  $\nu$  is total count rate for detector and  $\tau_d$  is a dead time (Vikhlinin et al. 1994; Zhang et al. 1995). Since the dead-time is not constant along energy band, we measured modified Poisson level for each extracted data-set separately.

Power spectrum of each of separate interval of *NuSTAR* observations has a form of a white noise plateau ( $P(f) \propto \text{const}$ ) on the low frequencies, transforming at the frequency  $\approx 0.1$  Hz in to the power law with the slope  $\rho \approx -1.6..-2.0$ . Also a prominent QPO at the frequencies 0.3–0.7 Hz and its second harmonic are present. Typical power spectrum of a single interval is shown in Fig. 6. From the shape of the energy and Fourier spectrum we concluded that the system is in the hard intermediate state and observed low frequency QPO (LF QPO) is of type C.

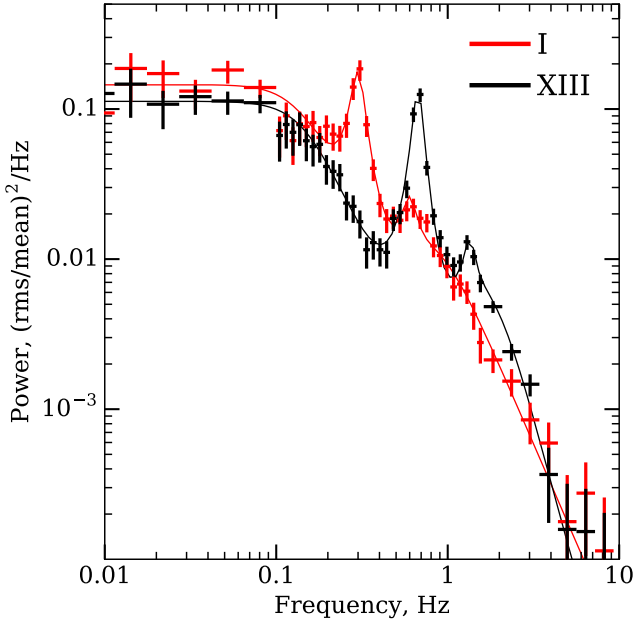


**Figure 6.** Power spectrum of the GRS 1739–278 obtained with *NuSTAR* data at the beginning (red crosses) and at the end (black crosses) of the observation. Poisson noise is subtracted.

For the light-curves extracted in 3–78 keV energy range Poisson noise dominates intrinsic source variability on the frequencies over  $\approx 1$  Hz, preventing analysis of any high-frequency features. There is also signs that the Power spectrum on the frequencies below  $\approx 0.003$  Hz has a form of growing power law  $P(f) \propto f^\alpha$ ,  $\alpha > 0.3$ . We did not try to find any high frequency QPOs, since the typical HF QPO (centroid frequency 100–400 Hz, amplitude  $\approx 10\%$  and quality  $Q \approx 2$ –10) is indiscernible over the Poisson noise with the obtained count-rate and duration of the observation.

In order to assess properties of GRS 1739–278 intrinsic variability we approximate each obtained power spectra with the following analytical function:

$$P(f) = n(1 + (f/f_{\text{lb}})^4)^\alpha + \frac{s_1}{(f - f_{\text{QPO}})^2 + (f_{\text{QPO}}/Q_m)^2} + \frac{s_2}{(f - 2f_{\text{QPO}})^2 + (2f_{\text{QPO}}/Q_m)^2} + \text{poiss} \quad (3)$$

Where  $f_{\text{lb}}$  - broad noise break frequency,  $f_{\text{QPO}}$  and  $Q_m$  - centroid of the QPO and its quality correspondingly and poiss - represents mean power of the variations caused by the counting statistics and dumped by dead-time. In this function first component represents plateau with the break, second two components describe QPO main harmonics and its overtone, last component represents constant Poisson noise. We take that the quality of the QPO harmonic is equal to the QPO peak quality. Further in the text will mention this models as standard.

We found that the QPO frequency had clearly evolved with time see Table 2 and Figure 6. The QPO frequency correlates with the *NuSTAR* flux and photon index, similar to many other black hole and neutron star binary systems

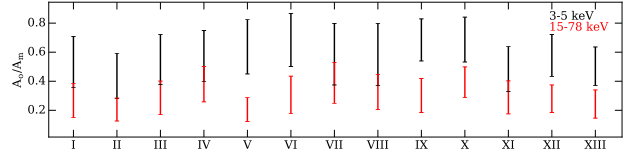


**Figure 7.** Ratio of the total power in the QPO and its second harmonic measured for the lightcurves obtained in 3–5 keV and 15–78 keV energy bands.

(see, e.g., Vignarca et al. 2003; Pottschmidt et al. 2003). On the other hand we see, that the QPO amplitude remained stable during the first half of the observation, and started to grow in the second part.

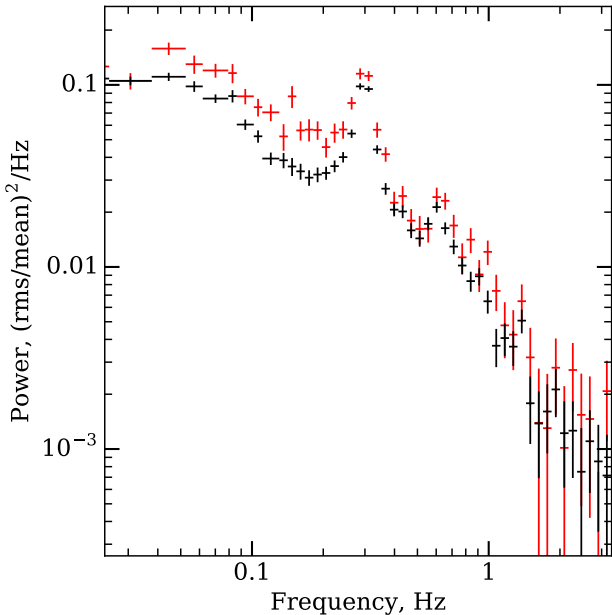
We found that the QPO amplitude is smaller in the soft band, while amplitude of its harmonic is bigger. The ratio of the power in the QPO and its harmonic for hard and soft energy bands is presented in Fig. 7. It follows that the QPO profile, if it is present (see, e.g. Ingram and van der Klis 2015), differs in the hard and soft X-ray bands. Following (Ingram and van der Klis 2015) we tried to extract QPO profile segregating the coherent part (Fourier signal with conserving phase shift relative to the signal on QPO frequency) between the QPO and its harmonics, however no significant coherence was presented above the noise level. It indicates that the QPO profile was not stable during the observation, in contradiction to the result obtained by Ingram and van der Klis (2015) for GRS 1915+105 with *RXTE* observatory data.

In some intervals QPO subharmonics, centered approximately at the 1/2 of the QPO centroid frequency, is clearly observed in the cospectra (see examples on Fig. 8, red crosses) (namely I, II, IV, V, VI sets). In order to observe QPO with better significance we stacked several cospectra, frequency of each cospectrum was scaled in such a way to conserve QPO centroid at 0.3 Hz. Obtained “tracked” cospectrum is presented on Fig. 8. The subharmonics seems to roam around the 1/2 QPO frequency, therefore we were not able to obtain it with a large significance on the tracked cospectrum.

It should be noted that the changes in the QPO centroid position during the interval may contribute to the observed quality factor  $Q$ . We can estimate the derivative of the QPO centroid position with time (by approximating  $f_{\text{QPO}}(\text{time})$  with the straight line), which appears to be  $\dot{f}_{\text{QPO}} \approx 5.0$ – $6.5 \times 10^{-6}$  Hz s $^{-1}$ . During an interval with the duration  $\tau = 3000$  s observed QPO drift will broaden the perfect periodic signal located at  $f_{\text{QPO}} = 0.3$  Hz up to the quality factor  $Q \approx f_{\text{QPO}}/(\dot{f}_{\text{QPO}}\tau) \approx 17$ , which is of order of the  $Q$  estimations obtained from the observations with standard model (described with eq.3). In order to better estimate the QPO quality factor, we split each of the 13 intervals in sets of 82 s long time-series. After that, for each of 13 intervals, we fitted obtained power spectra simultaneously with new model in which we assume that QPO frequency linearly growing with time. The model has the same form as standard with  $f_{\text{QPO}}$  substituted with  $\dot{f}_{\text{QPO}} = f_{\text{QPO}} + (t - t_{\text{mid}})\dot{f}_{\text{QPO}}$ , where  $f_{\text{QPO}}$  is the free parameter and  $t_{\text{mid}}$ ,  $f_{\text{QPO}}$  are the middle time of the  $i$ -th 82 s interval and QPO centroid frequency measured with standard model correspondingly. Inside each data set

**Table 2.** Evolution of the Fourier and energy spectrum properties through the *NuSTAR* observation in the 3–78 keV energy band.

Interval	$T_{start}$ , MJD	Expo, s	$f_{br}$ , $\times 10^{-2}$ , Hz	$f_{QPO}$ , Hz	$Q_m$ ,	$A_m$ , %	$A_o$ , %	rms %	$\Gamma$	$E_{cut}$ , keV
I	56742.68	3386	$8.9^{+2.2}_{-2.3}$	$0.30 \pm 0.01$	$15^{+5}_{-3}$	$7.5^{+0.9}_{-1.0}$	$2.7^{+0.8}_{-0.9}$	$26 \pm 1$	$1.459 \pm 0.005$	$29.9 \pm 0.4$
II	56742.75	3388	$7.8^{+2.0}_{-1.8}$	$0.31 \pm 0.01$	$13 \pm 3$	$7.9^{+0.9}_{-1.0}$	$2.7^{+0.8}_{-0.9}$	$26 \pm 1$	$1.462 \pm 0.005$	$30.7 \pm 0.4$
III	56742.82	3392	$8.2^{+2.4}_{-1.9}$	$0.34 \pm 0.01$	$12^{+3}_{-2}$	$7.7^{+0.9}_{-0.8}$	$3.9^{+0.9}_{-0.8}$	$26 \pm 1$	$1.464 \pm 0.005$	$29.7 \pm 0.4$
IV	56742.88	3389	$8.3^{+2.0}_{-1.8}$	$0.35 \pm 0.01$	$15^{+4}_{-3}$	$7.6 \pm 0.9$	$3.2^{+0.7}_{-0.8}$	$26 \pm 1$	$1.468 \pm 0.005$	$29.5^{+0.4}_{-0.3}$
V	56742.95	3389	$6.9^{+1.6}_{-1.4}$	$0.39 \pm 0.01$	$13^{+4}_{-3}$	$7.4 \pm 0.8$	$4.3^{+0.8}_{-0.9}$	$26 \pm 1$	$1.473 \pm 0.005$	$28.6 \pm 0.3$
VI	56743.02	3136	$7.5^{+1.9}_{-1.5}$	$0.41 \pm 0.01$	$17^{+5}_{-3}$	$6.9^{+0.9}_{-0.8}$	$3.8^{+0.7}_{-0.8}$	$26 \pm 1$	$1.475 \pm 0.005$	$28.1 \pm 0.3$
VII	56743.09	2771	$9.7^{+2.7}_{-2.2}$	$0.43 \pm 0.01$	$12^{+3}_{-2}$	$7.4 \pm 0.9$	$3.6 \pm 0.9$	$26^{+2}_{-1}$	$1.500 \pm 0.005$	$28.7 \pm 0.4$
VIII	56743.15	3387	$5.8^{+1.4}_{-1.5}$	$0.46 \pm 0.01$	$11^{+3}_{-2}$	$7.9 \pm 0.9$	$4.2^{+0.9}_{-0.8}$	$27 \pm 2$	$1.507 \pm 0.005$	$29.3 \pm 0.4$
IX	56743.22	3392	$7.1^{+1.6}_{-1.4}$	$0.50 \pm 0.01$	$12^{+4}_{-3}$	$7.9 \pm 0.8$	$4.3 \pm 0.8$	$26 \pm 1$	$1.504 \pm 0.005$	$28.1 \pm 0.3$
X	56743.29	3390	$7.0^{+1.7}_{-1.6}$	$0.53 \pm 0.01$	$13^{+3}_{-2}$	$8.7 \pm 0.7$	$4.5^{+0.7}_{-0.8}$	$25 \pm 1$	$1.498 \pm 0.005$	$27.2 \pm 0.3$
XI	56743.35	3382	$(6.7 \pm 1.5)$	$0.57 \pm 0.01$	$13 \pm 3$	$9.1^{+0.8}_{-0.7}$	$4.0 \pm 0.8$	$25 \pm 1$	$1.527^{+0.004}_{-0.005}$	$28.7 \pm 0.3$
XII	56743.42	3386	$6.7^{+1.8}_{-1.4}$	$0.63 \pm 0.01$	$14^{+3}_{-2}$	$9.5^{+0.8}_{-0.7}$	$4.4 \pm 0.7$	$26^{+2}_{-1}$	$1.525 \pm 0.004$	$27.5 \pm 0.3$
XIII	56743.49	3391	$7.5^{+1.7}_{-1.5}$	$0.67 \pm 0.01$	$15 \pm 3$	$9.6 \pm 0.7$	$4.2 \pm 0.8$	$25^{+2}_{-1}$	$1.528 \pm 0.004$	$26.2 \pm 0.3$

**Figure 8.** Cross-spectrum of the observations, obtained by scaling frequency to conserve QPO position. Black crosses obtained from the all intervals, while red crosses are from intervals I, II, IV, and V, in which QPO subharmonics was most prominent.

we obtained the QPO centroid changing speed consistent with the estimation obtained from the general trend ( $\approx 2\text{--}9 \times 10^{-6} \text{ Hz s}^{-1}$ ), nevertheless the median quality factor, obtained in this model appears to be  $\sim 14.3$  - i.e. compatible with the previous estimations made with standard model (see Table 2). It should be noted that the estimation of the QPO quality factor is restricted by the width of fast Fourier transform frequency bins, which is  $1/T$ , where  $T$  - is a duration of separate series used for fitting, in our case  $T = 82 \text{ s}$ , and QPO width is limited at  $1/T = 0.012 \text{ Hz}$  (we can not discriminate  $Q > 25$ ).

## 5.2 Coherence

Vaughan and Nowak (1997) suggested to use coherence between different energy bands in order to obtain additional information from the source variability. Coherence measure the similarity between two signals and can be computed with the following expression:

$$C(f) = \frac{|\langle F_s(f) * F_h(f) \rangle|^2 - n^2}{\langle |F_s(f)|^2 \rangle \langle |F_h(f)|^2 \rangle} \quad (4)$$

where  $F_h(f)$  and  $F_s(f)$  are Fourier function (corrected for the Poisson noise components) of the observed time series in hard and soft bands, correspondingly,  $n^2$  - product of the power in uncorrelated components, connected with counting statistic, divided by the number of used series (Vaughan and Nowak 1997). Coherence should be computed for the number of independent time series, therefore we separated each of the available uninterrupted time intervals on several shorter parts, 82 s long each.

Coherence is very similar to cospectrum, but instead of tracking signals with zero phase shifts, it tracks all signals with arbitrary conserved phase shift - i.e. Fourier harmonics of the signals may delay each other but be coherent (which means that Fourier functions  $F_h(f)$  and  $F_s(f)$  are related by linear transformation (Vaughan and Nowak 1997)).

Different models of the XBs variability generation suggest that the signals in two energy bands can be partially independent, while the shape of the power spectra is conserved. It appears that in many sources coherence between soft and hard X-ray bands is close to unity (Nowak et al. 1999; Wijnands and van der Klis 1999), however there also were indications on complex picture of the coherence in particular state of some systems (Ji et al. 2003), or drop in coherence between particular energy bands (e.g. in GX 339-4 Vaughan and Nowak 1997). See also discussion in the Vaughan and Nowak (1997) for the theoretical prediction on the coherence for different models.

Following Vaughan and Nowak (1997), we estimated correlation of GRS 1739-278 light-curves obtained in different soft and hard energy bands. Since for the timing analysis we use *NuSTAR* data, covering 3–78 keV energy band, we adopted following energy bands for our analysis: 3–5 keV,



5–8 keV, 8–15 keV and 15–78 keV. This partition of the *NuSTAR* energy band pursues the following idea: despite the energy spectrum of GRS 1739–278 can be described with the two major components - powerlaw continuum and fluorescent Fe K $\alpha$  line, we can expect that each of the chosen energy bands is dominated by the processes with slightly different origin. The Fe K $\alpha$  line has equivalent width approximately 0.2 keV, therefore producing only 5% of the flux in the 5–8 keV and must be anchored to some source of the hard photons depending on the system geometry, e.g. in the lamp post geometry it should be coherent with the hard powerlaw emission. In the 8–15 keV energy band we expecting the hard powerlaw corona emission to be dominant, while in the 15–78 keV Compton hump is present.

Since the *NuSTAR* detectors have complex dead-time depending on energy (see [Bachetti et al. 2015](#), for a details on how this affects power spectra), coherence computed from one detector is subject to the dead-time crosstalk effects (which should make random processes more coherent). In order to eliminate this effects, following the recipe suggested in [Bachetti et al. \(2015\)](#) for cospectrum estimation, for the numerator in Eq. 4 we used cross-products of the light-curves Fourier functions obtained from the different modules - e.g. correlations of the light-curve obtained in the soft band on the FPMA module with the light-curve in the hard band obtained on the FPMB module and vice versa. In the obtained cross-product dead-time cross-talk effects are significantly dumped. We also used cospectrum obtained for each energy band as the estimation for the denominator in the Eq. 4. The  $n^2$  component was computed as it is suggested by [Vaughan and Nowak \(1997\)](#), however for the Poisson noise components power estimation we used mean value of the power spectra in the 5–15 Hz range, assuming that Poisson noise dominating intrinsic source variability and is constant along frequencies.

[Wijnands and van der Klis \(1999\)](#) shown that primary features of the power spectrum of the XBs in low-hard state are evolving simultaneously, i.e. flat top broad band noise break frequency and QPO centroid frequency are connected with the relation  $f_b \approx 0.3f_{\text{QPO}}$ . Bearing in mind aforementioned property of the power spectrum, despite observed scatter in the  $f_b/f_{\text{QPO}}$  in our data, in order to improve significance of the coherence measurements we stacked all 13 separate intervals of the observation, scaling their frequencies to preserve QPO position. We assumed that the coherence in each tracked frequency channel is preserved along the observation.

The coherence between hard and soft energy bands at frequencies up to  $\sim 3$  Hz is presented in Fig. 9. We found that coherence in the adjacent energy bands is close to unity, with mean values in 0.01–1 Hz frequency band being  $1.0 \pm 0.05$ , however for the 3–5 and 15–78 keV energy bands the coherence is significantly lower, see Fig. 9. It is on the nearly constant level of  $\approx 0.85$  in the  $5 \times 10^{-3}$ –0.1 Hz frequency band and drops down above this frequency.

### 5.3 Phase lags

From the definition of the coherence (see eq. 4) it follows that signals have roughly constant phase shifts between their Fourier functions in each frequency bin where they are coherent. Following [Vaughan and Nowak \(1997\)](#) we estimated

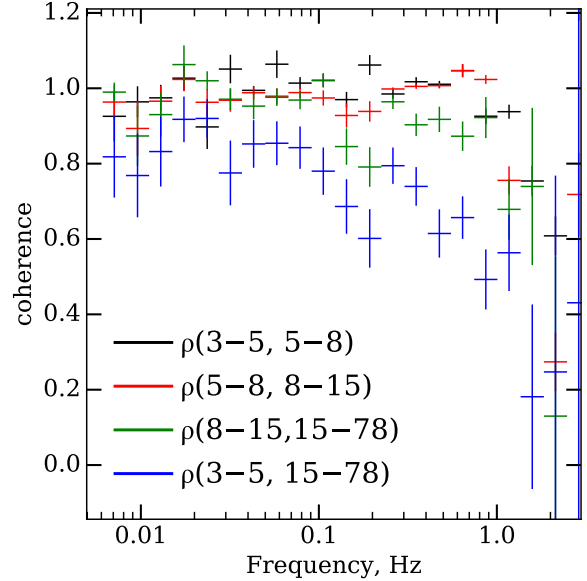


**Figure 9.** Coherence between different energy bands: red crosses between 3–5 and 5–8 keV, green crosses between 5–8 and 8–15 keV, blue crosses between 8–15 and 15–78 keV, black crosses between 3–5 and 15–78 keV.

phase lag as an angle of mean product of the light curves Fourier harmonics from one energy bands to the conjugated Fourier harmonics of the second energy band.

$$\delta\phi(f) = \arctan \left( \frac{\text{Im}(\langle F_s^*(f)F_h^*(f) \rangle)}{\text{Re}(\langle F_s^*(f)F_h^*(f) \rangle)} \right) \quad (5)$$

For the error estimation we used [Uttley et al. \(2014\)](#) approach, therefore  $\Delta\delta\phi = \arctan(\Delta\gamma^2/\gamma^2)$ , where  $\gamma^2$  - estimation of the coherence, and  $\Delta\gamma^2$  is coherence error estimation. It should be noted that this estimation of the error is build on the assumption that each product  $\langle F_h^*(f)F_s^*(f) \rangle$  can be represented as a sum of randomly (for uncoherent signals) and particularly oriented (for coherent signals) vectors with constant length on complex plane, while it can be shown that, at least for uncoherent signals, that the length of this vectors is also random variable with Laplace distribution ([Huppenkothen and Bachetti 2017](#)).

We computed the phase lag spectrum with two approaches - with and without QPO centroid frequency tracing (see right and left panels of Fig.10 correspondingly). It appears that in the 0.1–3 Hz frequency band positive (hard) lag is present, on the frequencies below 0.1 Hz there are indication on the negative (soft) lag. Observed phase lag corresponds to the delay times between soft and hard photons  $\sim 0.1$  s for frequencies above 0.1 Hz and  $-0.1$ – $-1$  s for frequencies below 0.1 Hz.

[Zhang et al. \(2017\)](#) shown that the phase lag at the QPO frequency and its second harmonic in GX 339-4 BHC evolves with this frequency. It is also was shown by different authors (see, e.g., [Pahari et al. 2013](#); [Zhang et al. 2017](#)) that some distinct features are usually presented in phase lag spectra on the QPO and its harmonics frequencies, however, our signal to noise ratio appears to be insufficient to determine

**Table 3.** QPOs detected in *Swift-XRT* observations

Segment	$f_{QPO}$ , Hz	$rms$ , %	Type
03	0.4	14%	C
04	2.2	11%	B
05	1.7	13%	B
06	5.0	6%	B
07	2.5	10%	B
08	5.1	7%	B
09	2.2	11%	B

the presence of such features. (van den Eijnden et al. 2017) shown that the sign of the phase lag on the type-C QPO centroid frequency depends on a system inclination, however this difference is explicit only when QPO centroid frequency is above  $\sim 3$  Hz.

#### 5.4 *Swift-XRT* observations

We performed search for LF QPOs in first dozen of *Swift-XRT* observations of the GRS 1739–278. QPO is clearly detected in observations 3 to 9, with frequency varying from 0.4 Hz (during simultaneous observation with *NuSTAR*, see Fig. 2) up to 5 Hz (see Tab. 3). We used shape of power spectrum in order to classify QPOs as belonging to type C or B. Except for the first detection (observation 03) power spectra were red-noise like without strong low-frequency components, which is typical for type-B QPOs in soft-intermediate state. Observed frequencies of these QPOs are range from  $\sim 2$  Hz to 5 Hz, similar to what had been observed in GX 339-4 (Motta et al. 2011). We calculated  $rms$  for each detected QPO - most of them is higher than 10%, which is not typical for type C QPO (Casella et al. 2005).

## 6 DISCUSSION AND CONCLUSIONS

We had studied the spectro-timing evolution of GRS 1739–278 during its hard-intermediate state. We found a prominent type-C LF QPO in its power spectrum, its frequency show clear correlation with parameters of continuum emission. As the QPO frequency increases from 0.3 to 0.7 Hz spectrum became softer: the power law index grows from 1.46 to 1.53 and cut-off energy decreases from 30 to 26 keV. Overall flux increases, too. Such behaviour was first observed in a number of systems by Di Matteo and Psaltis (1999) and now it is studied in greater details in many systems (see e.g. Vignarca et al. 2003; Stiele et al. 2013; Seifina et al. 2014; Fürst et al. 2016, and many more). Although the quality of a data prevented us from measuring a movement of the inner disk boundary, from the total broadband spectrum we found that an accretion disk is truncated at radius smaller than  $9 GM/c^2$  (90% confidence limit) which is in agreement with an estimates by Miller et al. (2015). We used this combination of inner radius and QPO together with Lense-Thirring precession model of QPO origin (Ingram et al. 2009) in order to assess black hole mass. Following Ingram and Motta (2014) we calculated nodal frequencies (which is thought to correspond to QPO fundamental frequency) versus inner radius for two values of the black hole mass ( $10M_\odot$  and  $30M_\odot$ ) and

two values of spin -  $a = 0.1$  and  $a = 0.998$  (maximally rotating). As it can be seen from Fig. 11 observations are incompatible with black hole mass  $10M_\odot$  and barely agrees with slowly rotating massive black hole. This results, along with measurements by Fürst et al. (2016), indicate that there are some tensions between predictions of RPM and truncation radii inferred from spectral fitting.

We carried out extensive study of timing properties of the GRS 1739–278. Along with the broadband noise and fundamental QPO, second harmonic of QPO is clearly seen. During several intervals from first half of the observation subharmonic is also observed. In all 13 intervals second QPO harmonic is more prominent in soft band (3–5 keV), with ratio of its amplitude to that of fundamental QPO being  $0.565 \pm 0.02$  in 3–5 keV band versus  $0.275 \pm 0.02$  in 15–78 keV. We also measured velocity of the QPO drift and found it to be  $\approx 6.0 \times 10^{-6}$  Hz s $^{-1}$ . We searched for similar QPO in *Swift-XRT* observations of GRS 1739–278 performed after *NuSTAR* exposure and found that all other detected QPOs are probably of type B, thus indicating that the type-C QPO reach saturation on frequencies below few Hz. Coherence measured between adjacent energy ranges in 0.01-1 Hz was found to be nearly unity, while for distant energy bands coherence turned out to be lower. Phase lag found to be of order of +0.1 s (hard) in the 0.1–3 Hz frequency range and  $-1..-0.1$  s (soft) below 0.1 Hz.

## ACKNOWLEDGMENTS

The work was supported by the Russian Science Foundation (grant no. 14-12-01287). Authors are grateful for T.Dauser and J.Gracia for their help with *relxill* model. This research has made use of data obtained through the High Energy Astrophysics Science Archive Research Center Online Service, provided by the NASA/Goddard Space Flight Center.

## REFERENCES

- Allen, C. W.: 1973, *Astrophysical quantities*
- Arévalo, P. and Uttley, P.: 2006, *MNRAS* **367**, 801
- Arnaud, K. A.: 1996, in G. H. Jacoby and J. Barnes (eds.), *Astronomical Data Analysis Software and Systems V*, Vol. 101 of *Astronomical Society of the Pacific Conference Series*, p. 17
- Bachetti, M., Harrison, F. A., Cook, R., Tomsick, J., Schmid, C., Grefenstette, B. W., Barret, D., Boggs, S. E., Christensen, F. E., Craig, W. W., Fabian, A. C., Fürst, F., Gandhi, P., Hailey, C. J., Kara, E., Maccarone, T. J., Miller, J. M., Pottschmidt, K., Stern, D., Uttley, P., Walton, D. J., Wilms, J., and Zhang, W. W.: 2015, *ApJ* **800**, 109
- Belloni, T. and Hasinger, G.: 1990, *A&A* **227**, L33
- Belloni, T. M.: 2010, in T. Belloni (ed.), *Lecture Notes in Physics*, Berlin Springer Verlag, Vol. 794 of *Lecture Notes in Physics*, Berlin Springer Verlag, p. 53
- Belloni, T. M. and Motta, S. E.: 2016, in C. Bambi (ed.), *Astrophysics of Black Holes: From Fundamental Aspects to Latest Developments*, Vol. 440 of *Astrophysics and Space Science Library*, p. 61
- Borozdin, K. N., Revnivtsev, M. G., Trudolyubov, S. P., Aleksandrovich, N. L., Sunyaev, R. A., and Skinner, G. K.: 1998, *Astronomy Letters* **24**, 435
- Borozdin, K. N. and Trudolyubov, S. P.: 2000, *ApJ* **533**, L131
- Cabanac, C., Henri, G., Petrucci, P.-O., Malzac, J., Ferreira, J., and Belloni, T. M.: 2010, *MNRAS* **404**, 738

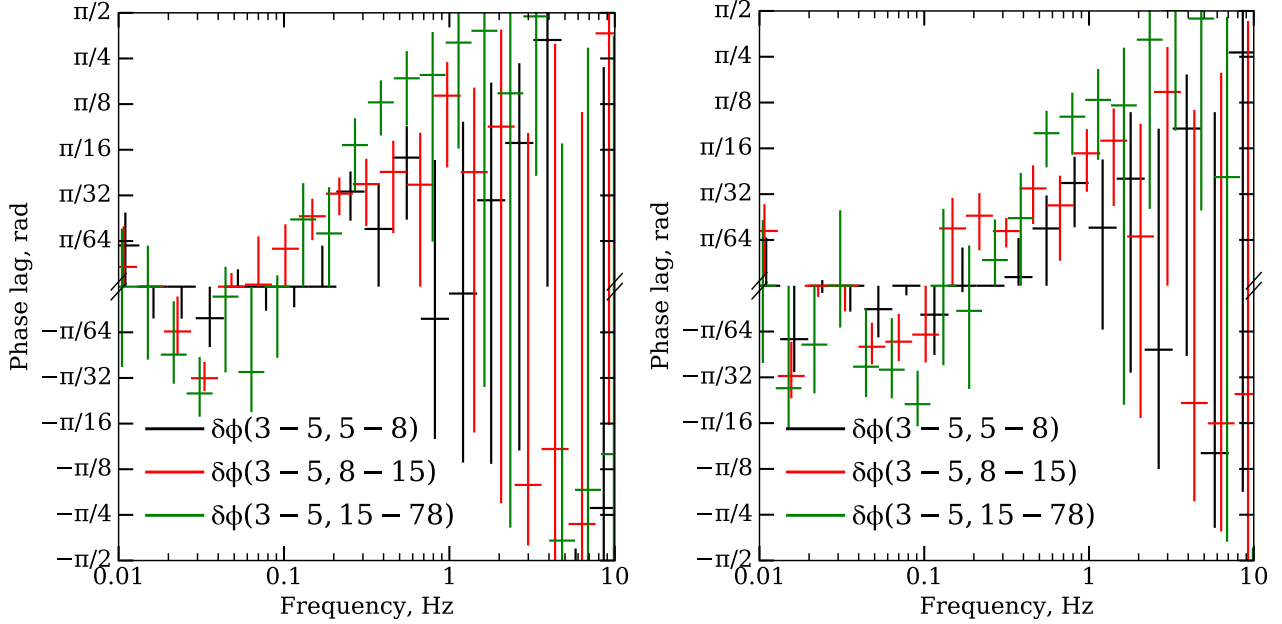


**Figure 10.** Phase lag between the soft (3–5 keV) and hard (5–8; 8–15; 15–78 keV) energy bands in GRS 1739–278. On the left panel - phase lag spectrum obtained from *NuSTAR* observations by stacking all data, on the right panel same spectrum with tracked frequency (frequency for each separate light-curve segment was scaled such a way to conserve QPO centroid at 0.3 Hz).

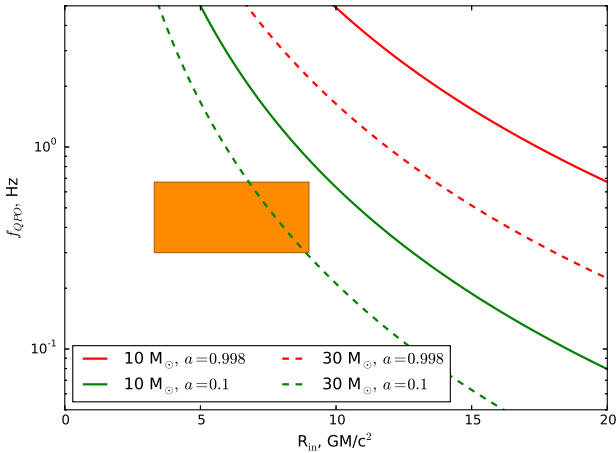


**Figure 11.** Expected QPO frequency for a black hole of a given mass and spin versus inner disk radius from Ingram and Motta (2014). Orange square represent region containing observed QPOs.

Casella, P., Belloni, T., and Stella, L.: 2005, *ApJ* **629**, 403  
 Churazov, E., Gilfanov, M., and Revnivtsev, M.: 2001, *MNRAS* **321**, 759  
 Dauser, T., García, J., Parker, M. L., Fabian, A. C., and Wilms, J.: 2014, *MNRAS* **444**, L100  
 Dauser, T., García, J., Walton, D. J., Eikmann, W., Kallman, T., McClintock, J., and Wilms, J.: 2016, *A&A* **590**, A76  
 Di Matteo, T. and Psaltis, D.: 1999, *ApJ* **526**, L101  
 Dickey, J. M. and Lockman, F. J.: 1990, *ARA&A* **28**, 215  
 Eardley, D. M., Lightman, A. P., and Shapiro, S. L.: 1975, *ApJ* **199**, L153  
 Evans, P. A., Beardmore, A. P., Page, K. L., Osborne, J. P., O'Brien, P. T., Willingale, R., Starling, R. L. C., Burrows,

D. N., Godet, O., Vetere, L., Racusin, J., Goad, M. R., Wiersema, K., Angelini, L., Capalbi, M., Chincarini, G., Gehrels, N., Kennea, J. A., Margutti, R., Morris, D. C., Mountford, C. J., Pagani, C., Perri, M., Romano, P., and Tanvir, N.: 2009, *MNRAS* **397**, 1177  
 Filippova, E., Kuulkers, E., Skådt, N. M., Alfonso-Garzon, J., Beckmann, V., Bird, A. J., Brandt, S., Chenevez, J., Del Santo, M., Domingo, A., Ebisawa, K., Jonker, P. G., Kretschmar, P., Markwardt, C. B., Oosterbroek, T., Paizis, A., Pottschmidt, K., Sanchez-Fernandez, C., Wijnands, R., Bozzo, E., and Ferrigno, C.: 2014, *The Astronomer's Telegram* 5991  
 Fuerst, F., Tomsick, J. A., Yamaoka, K., Dauser, T., Miller, J. M., Clavel, M., Corbel, S., Fabian, A. C., Garcia, J., Harrison, F. A., Loh, A., Kaaret, P., Kalemci, E., Migliari, S., Miller-Jones, J. C. A., Pottschmidt, K., Rahoui, F., Rodriguez, J., Stern, D., Stuhlinger, M., Walton, D. J., and Wilms, J.: 2016, *ArXiv e-prints*  
 Fürst, F., Grinberg, V., Tomsick, J. A., Bachetti, M., Boggs, S. E., Brightman, M., Christensen, F. E., Craig, W. W., Gandhi, P., Grefenstette, B., Hailey, C. J., Harrison, F. A., Madsen, K. K., Parker, M. L., Pottschmidt, K., Stern, D., Walton, D. J., Wilms, J., and Zhang, W. W.: 2016, *ApJ* **828**, 34  
 García, J., Dauser, T., Reynolds, C. S., Kallman, T. R., McClintock, J. E., Wilms, J., and Eikmann, W.: 2013, *ApJ* **768**, 146  
 Gierliński, M., Middleton, M., Ward, M., and Done, C.: 2008, *Nature* **455**, 369  
 Grebenev, S. A., Sunyaev, R. A., and Pavlinsky, M. N.: 1997, *Advances in Space Research* **19**, 15  
 Greiner, J., Dennerl, K., and Predehl, P.: 1996, *A&A* **314**, L21  
 Harrison, F. A., Craig, W. W., Christensen, F. E., Hailey, C. J., Zhang, W. W., Boggs, S. E., Stern, D., Cook, W. R., Forster, K., Giommi, P., Grefenstette, B. W., Kim, Y., Kitaguchi, T., Koglin, J. E., Madsen, K. K., Mao, P. H., Miyasaka, H., Mori, K., Perri, M., Pivovarov, M. J., Puccetti, S., Rana, V. R., Westergaard, N. J., Willis, J., Zoglauer, A., An, H., Bachetti, M., Barrière, N. M., Bellm, E. C., Bhalerao, V., Brejnholt,

- N. F., Fuerst, F., Liebe, C. C., Markwardt, C. B., Nynka, M., Vogel, J. K., Walton, D. J., Wik, D. R., Alexander, D. M., Cominsky, L. R., Hornschemeier, A. E., Hornstrup, A., Kaspi, V. M., Madejski, G. M., Matt, G., Molendi, S., Smith, D. M., Tomsick, J. A., Ajello, M., Ballantyne, D. R., Baloković, M., Barret, D., Bauer, F. E., Blandford, R. D., Brandt, W. N., Brenneman, L. W., Chiang, J., Chakrabarty, D., Chenevez, J., Comastri, A., Dufour, F., Elvis, M., Fabian, A. C., Farrah, D., Fryer, C. L., Gotthelf, E. V., Grindlay, J. E., Helfand, D. J., Krivonos, R., Meier, D. L., Miller, J. M., Natalucci, L., Ogle, P., Ofek, E. O., Ptak, A., Reynolds, S. P., Rigby, J. R., Tagliaferri, G., Thorsett, S. E., Treister, E., and Urry, C. M.: 2013, *ApJ* **770**, 103
- Heil, L. M., Uttley, P., and Klein-Wolt, M.: 2015, *MNRAS* **448**, 3339
- Hjellming, R. M., Rupen, M. P., Marti, J., Mirabel, F., and Rodriguez, L. F.: 1996, *IAU Circ.* 6383
- Homan, J. and Belloni, T.: 2005, *Ap&SS* **300**, 107
- Homan, J., Wijnands, R., van der Klis, M., Belloni, T., van Paradijs, J., Klein-Wolt, M., Fender, R., and Méndez, M.: 2001, *ApJS* **132**, 377
- Huppenkothen, D. and Bachetti, M.: 2017, *ArXiv e-prints*
- Ingram, A., Done, C., and Fragile, P. C.: 2009, *MNRAS* **397**, L101
- Ingram, A. and Motta, S.: 2014, *MNRAS* **444**, 2065
- Ingram, A. and van der Klis, M.: 2013, *MNRAS* **434**, 1476
- Ingram, A. and van der Klis, M.: 2015, *MNRAS* **446**, 3516
- Ingram, A., van der Klis, M., Middleton, M., Done, C., Altamirano, D., Heil, L., Uttley, P., and Axelsson, M.: 2016, *MNRAS* **461**, 1967
- James, F. and Roos, M.: 1975, *Comput. Phys. Commun.* **10**, 343
- Ji, J. F., Zhang, S. N., Qu, J. L., and Li, T. P.: 2003, *ApJ* **584**, L23
- Kalberla, P. M. W., Burton, W. B., Hartmann, D., Arnal, E. M., Bajaja, E., Morras, R., and Pöppel, W. G. L.: 2005, *A&A* **440**, 775
- Krimm, H. A., Barthelmy, S. D., Baumgartner, W., Cummings, J., Gehrels, N., Lien, A. Y., Markwardt, C. B., Palmer, D., Sakamoto, T., Stamatikos, M., and Ukwatta, T.: 2014, *The Astronomer's Telegram* 5986
- Krimm, H. A., Holland, S. T., Corbet, R. H. D., Pearlman, A. B., Romano, P., Kennea, J. A., Bloom, J. S., Barthelmy, S. D., Baumgartner, W. H., Cummings, J. R., Gehrels, N., Lien, A. Y., Markwardt, C. B., Palmer, D. M., Sakamoto, T., Stamatikos, M., and Ukwatta, T. N.: 2013, *ApJS* **209**, 14
- Lyubarskii, Y. E.: 1997, *MNRAS* **292**, 679
- Marshall, D. J., Robin, A. C., Reylé, C., Schultheis, M., and Picaud, S.: 2006, *A&A* **453**, 635
- Marti, J., Mirabel, I. F., Duc, P.-A., and Rodriguez, L. F.: 1997, *A&A* **323**, 158
- Matsuoka, M., Kawasaki, K., Ueno, S., Tomida, H., Kohama, M., Suzuki, M., Adachi, Y., Ishikawa, M., Mihara, T., Sugizaki, M., Isobe, N., Nakagawa, Y., Tsunemi, H., Miyata, E., Kawai, N., Kataoka, J., Morii, M., Yoshida, A., Negoro, H., Nakajima, M., Ueda, Y., Chujo, H., Yamaoka, K., Yamazaki, O., Nakahira, S., You, T., Ishiwata, R., Miyoshi, S., Eguchi, S., Hiroi, K., Katayama, H., and Ebisawa, K.: 2009, *PASJ* **61**, 999
- Mauche, C. W.: 2002, *ApJ* **580**, 423
- Mereminskiy, I. A., Filippova, E. V., Krivonos, R. A., Grebenev, S. A., Burenin, R. A., and Sunyaev, R. A.: 2017, *Astronomy Letters* **43**, 167
- Miller, J. M., Homan, J., and Miniutti, G.: 2006a, *ApJ* **652**, L113
- Miller, J. M., Homan, J., Steeghs, D., Rupen, M., Hunstead, R. W., Wijnands, R., Charles, P. A., and Fabian, A. C.: 2006b, *ApJ* **653**, 525
- Miller, J. M., Tomsick, J. A., Bachetti, M., Wilkins, D., Boggs, S. E., Christensen, F. E., Craig, W. W., Fabian, A. C., Grefenstette, B. W., Hailey, C. J., Harrison, F. A., Kara, E., King, A. L., Stern, D. K., and Zhang, W. W.: 2015, *ApJ* **799**, L6
- Miyamoto, S., Kitamoto, S., Iga, S., Negoro, H., and Terada, K.: 1992, *ApJ* **391**, L21
- Molteni, D., Sponholz, H., and Chakrabarti, S. K.: 1996, *ApJ* **457**, 805
- Motta, S., Muñoz-Darias, T., Casella, P., Belloni, T., and Homan, J.: 2011, *MNRAS* **418**, 2292
- Narayan, R. and Yi, I.: 1995, *ApJ* **452**, 710
- Nowak, M. A., Wilms, J., and Dove, J. B.: 1999, *ApJ* **517**, 355
- Pahari, M., Neilsen, J., Yadav, J. S., Misra, R., and Uttley, P.: 2013, *ApJ* **778**, 136
- Parker, M. L., Tomsick, J. A., Miller, J. M., Yamaoka, K., Lohfink, A., Nowak, M., Fabian, A. C., Alston, W. N., Boggs, S. E., Christensen, F. E., Craig, W. W., Fürst, F., Gandhi, P., Grefenstette, B. W., Grinberg, V., Hailey, C. J., Harrison, F. A., Kara, E., King, A. L., Stern, D., Walton, D. J., Wilms, J., and Zhang, W. W.: 2015, *ApJ* **808**, 9
- Paul, J., Bouchet, L., Churazov, E., and Sunyaev, R.: 1996, *IAU Circ.* 6348
- Paul, J., Mandrou, P., Ballet, J., Cantin, M., Chabaud, J., Cordier, B., Ehanno, M., Goldwurm, A., Lambert, A., Lande, J., et al.: 1991, *Advances in Space Research* **11**(8), 289
- Pottschmidt, K., Wilms, J., Nowak, M. A., Pooley, G. G., Gleissner, T., Heindl, W. A., Smith, D. M., Remillard, R., and Staubert, R.: 2003, *A&A* **407**, 1039
- Remillard, R. A. and McClintock, J. E.: 2006, *ARA&A* **44**, 49
- Revnivtsev, M., Gilfanov, M., and Churazov, E.: 2000, *A&A* **363**, 1013
- Ross, R. R. and Fabian, A. C.: 2005, *MNRAS* **358**, 211
- Schultheis, M., Chen, B. Q., Jiang, B. W., Gonzalez, O. A., Enokiya, R., Fukui, Y., Torii, K., Rejkuba, M., and Minniti, D.: 2014, *A&A* **566**, A120
- Seifina, E., Titarchuk, L., and Shaposhnikov, N.: 2014, *ApJ* **789**, 57
- Shakura, N. I. and Sunyaev, R. A.: 1973, *A&A* **24**, 337
- Shapiro, S. L., Lightman, A. P., and Eardley, D. M.: 1976, *ApJ* **204**, 187
- Stella, L. and Vietri, M.: 1998, *ApJ* **492**, L59
- Stiele, H., Belloni, T. M., Kalemci, E., and Motta, S.: 2013, *MNRAS* **429**, 2655
- Tagger, M. and Pellat, R.: 1999, *A&A* **349**, 1003
- Tanaka, Y. and Shibazaki, N.: 1996, *ARA&A* **34**, 607
- Terrell, Jr., N. J.: 1972, *ApJ* **174**, L35
- García, J., Dauser, T., Lohfink, A., Kallman, T. R., Steiner, J. F., McClintock, J. E., Brenneman, L., Wilms, J., Eikmann, W., Reynolds, C. S., and Tombesi, F.: 2014, *ApJ* **782**, 76
- Uttley, P., Cackett, E. M., Fabian, A. C., Kara, E., and Wilkins, D. R.: 2014, *A&ARv* **22**, 72
- van den Eijnden, J., Ingram, A., Uttley, P., Motta, S. E., Belloni, T. M., and Gardenier, D. W.: 2017, *MNRAS* **464**, 2643
- Vaughan, B. A. and Nowak, M. A.: 1997, *ApJ* **474**, L43
- Verner, D. A., Ferland, G. J., Korista, K. T., and Yakovlev, D. G.: 1996, *ApJ* **465**, 487
- Vignarca, F., Migliari, S., Belloni, T., Psaltis, D., and van der Klis, M.: 2003, *A&A* **397**, 729
- Vikhlinin, A., Churazov, E., and Gilfanov, M.: 1994, *A&A* **287**, 73
- Wijnands, R., Méndez, M., Miller, J. M., and Homan, J.: 2001, *MNRAS* **328**, 451
- Wijnands, R. and van der Klis, M.: 1999, *ApJ* **514**, 939
- Wilms, J., Allen, A., and McCray, R.: 2000, *ApJ* **542**, 914
- Yan, Z. and Yu, W.: 2017, *Monthly Notices of the Royal Astronomical Society* **470**(4), 4298
- Zhang, L., Wang, Y., Méndez, M., Chen, L., Qu, J., Altamirano, D., and Belloni, T.: 2017, *ApJ* **845**, 143
- Zhang, W., Jahoda, K., Swank, J. H., Morgan, E. H., and Giles, A. B.: 1995, *ApJ* **449**, 930

This paper has been typeset from a  $\text{\TeX}/\text{\LaTeX}$  file prepared by the author.